3D ROCK-PHYSICS TEMPLATES FOR ESTIMATING THE RESERVOIR PROPERTIES OF INTERBEDDED SANDSTONE AND SHALE THIN LAYERS

HONGJING DONG[1], JING BA[1]*, MENGBO ZHANG[2], JOSÉ M. CARCIONE[1, 3], MENGQIANG PANG[1] and WENHUI TAN[4]

[1]*School of Earth Sciences and Engineering, Hohai University, Nanjing 211100, P.R..China.*
[2]*Exploration and Development Research Institute of PetroChina Changqing Oilfield Company, Xi'an 710018, P.R. China.*
[3]*National Institute of Oceanography and Applied Geophysics – OGS, Trieste, Italy.*
[4]*Sinopec Geophysical Research Institute, Nanjing 211103, P.R. China.*

(Received June 6, 2023; revised version accepted January 16, 2024)

ABSTRACT

Dong, H.J., Ba, J., Zhang, M.B., Carcione, J.M., Pang, M.Q. and Tan, W.H., 2024. 3D rock-physics templates for estimating the reservoir properties of interbedded sandstone and shale thin layers. *Joutnal of Seismic Exploration*, 32: 509-532.

Shale oil has been considered an important resource for the global oil and gas industry in recent years. The Yanchang formations in the Ordos Basin, China, are characterized by rich oil reserves, complex structural features, low porosity, and low permeability, with developed microcracks and indistinct oil-water contacts. A rock-physics model (RPM) developed to interpret these features considers ten rock samples from the Chang-7 member to measure ultrasonic velocity, density, porosity, and permeability, and X-ray diffraction to obtain mineral composition and micropore structures. The Chang-7 member consists of interbedded thin layers of two lithologies (sandstone and shale). The proposed model is based on the Voigt-Reuss-Hill average (VRH), self-consistent approximation (SCA), differential effective medium (DEM) theory, and the squirt-flow and Gassmann equations, and analyzes the acoustic response in terms of various pore structures and mineral components. The model is tested with the measured P-wave (V_P) and S-wave (V_S) velocities, and multiscale 3D rock-physics templates of the sandstone and shale layers are built, and calibrated with ultrasonic, sonic (log) and seismic data. The spectral-ratio, centroid frequency-shift and its improved version are used to estimate the attenuation. Then, the templates are used to predict the properties of the two lithologies, showing good agreement with the log data and the production report.

KEY WORDS: shale-oil formations, tight-oil reservoir, rock-physics model, pore structure, attenuation.

0963-0651/23/$5.00

INTRODUCTION

With the increasing global demand for hydrocarbons and the scarcity of conventional oil/gas resources, unconventional hydrocarbon exploration has attracted increasing attention from the petroleum industry (Pang et al., 2015; Tan et al., 2020). Shale oil is considered as a complement to conventional oil/gas resources. The Chang-7 part of the Yanchang Formation in the Ordos Basin developed during the period of greatest lake inundation and consists of organic-rich shale and fine-grained sandstone deposits; it is the main target of unconventional oil exploration in the basin (Liang et al., 2020). The tight rocks in the formations have complex features, with thin interbeds of sandstone, shale, and mudstone, low porosity, low permeability, and strong heterogeneity (Feng et al., 2013; Fan et al., 2022).

Previous research has shown that microstructure heterogeneity can lead to diversity and complexity in rock-physical responses (Chapman et al., 2016; Ba et al., 2017; Dutilleul et al., 2020; Zhang et al., 2021). Sun et al. (2019) applied computed tomography (CT) to construct 3D digital cores and build a pore network model to analyze the effects of microfracture size, dip angle, and length on seepage properties. Ma and Ba (2020) calculated the scattering and intrinsic attenuation of tight rocks using the isotropic single scattering model and spectral-ratio method to analyze the effects of fluid saturation, pore structure, and mineral content. Experimental and theoretical studies have considered local fluid flow induced by seismic waves as the main cause of velocity dispersion and attenuation in rocks (Carcione et al., 2003; White, 1975; Spencer and Shine, 2016; Winker, 1985). Seismic attenuation has been used as an oil/gas indicator. Dasgupta and Clark (1998) analyzed field data and showed that seismic Q can be used to discriminate rock lithology. Brittleness is a key parameter for characterizing the fracability of tight reservoirs (Tan et al. 2018, Guo et al. 2013, Chen et al. 2014). Rocks with higher brittleness tend to form a complex network of fractures during fracturing, which favors fracturing practices and pore fluid extraction.

Rock-physics models (RPMs) simulate real rocks based on assumptions and establish the mutual relationships between wave behaviors and physical properties (Ba et al., 2017; Pang et al., 2019, 2022; Luo et al., 2023). Vernik and Nur (1992) established the RPM based on the Backus average and analyzed the effects of organic matter volume fraction, maturity, and other factors on shale anisotropy. Sayer (2005) analyzed the effects of clay mineral distribution on the elastic parameters of shale by proposing an RPM. Deng et al. (2015) studied the microstructural characterization of the Longmaxi Formation shale and established the corresponding seismic RPM, which provides a basis for predicting the sweet spot of the shale reservoir. Yang et al. (2017) analyzed the relationships between seismic responses and lithologies and included the effect of pore aspect ratio in the generation of RPM. Picotti et al. (2018) developed a rock-physics model of patchy saturation and used Q to quantitatively correlate seismic properties with porosity, permeability, and fluid saturation. Tan et al. (2020) and Ba et al. (2021) predicted reservoir brittleness based on seismic data and modeling.

Rock physical templates (RPTs) based on theoretical models can relate reservoir properties to elastic properties (Dvorkin and Mavko, 2006; Picotti et al., 2018; Carcione and Avseth, 2015; Li et al., 2019; Tan et al., 2020). A classical 2D RPT is based on phase velocity ratio (V_P /V_S ratio) and acoustic impedance to establish a quantitative relationship between wave response and saturation, lithology, and porosity (Odegaard and Avseth, 2004; Ba et al., 2013a, 2013b). Gupta et al. (2012) created an RPT using the Kuster-Toksöz model to detect thin sandstone reservoirs in the Cambay Basin and obtained an isobath map of the oil layer. Ba et al. (2013a, 2013b) create multiscale RPTs based on the equations of Biot-Rayleigh theory for detecting hydrocarbons in limestone reservoirs. Pang et al. (2020) considered microcrack porosity predicted by a 3D RPT to identify deep carbonate reservoirs.

The complex features of the lithology and pore structure of shale oil formations differ significantly from those of conventional reservoirs, and the pore spaces include intergranular pores and microcracks. In addition, the mineral composition in the target formations varies by depth and region. Therefore, the corresponding process of RPM also varies depending on depth or region. Pang et al. (2022) have shown that after analysing the characteristics of sandstone-shale strata, different models for different lithologies enables a reasonable prediction.

We collect ten samples of the shale-oil formations. Based on density, porosity and permeability measurements, ultrasonic tests, X-ray diffraction tests (XRD) and thin section analysis (CTS), the effects of mineral composition and microstructure on the elastic properties of the rocks are analyzed. The RPMs of sandstone and shale sublayers are proposed based on the Voigt-Reuss-Hill average (VRH), differential effective medium model (DEM), and self-consistent approximation (SCA), as well as squirt-flow model (Gurevich et al., 2010) and Gassmann equation (Gassmann, 1951). The changes in P-wave velocity and attenuation as a function of porosity, microcrack porosity, and clay content are analyzed. The multiscale 3D RPT of porosity, mineral composition and microcrack aspect ratio is established. The spectral-ratio method, centroid frequency-shift method and its improved version are used to estimate the ultrasonic, sonic (log) and seismic attenuation. In conjunction with the elastic properties, the RPTs are calibrated. Finally, the RPTs of two lithologies in the seismic frequency band are used to estimate the reservoir properties.

RESERVOIR CHARACTERISTICS AND MULTISCALE WAVE DATA

Geological characteristics of the work area

The Ordos Basin is one of the areas with rich hydrocarbon resources in China, located in the northern part of the North China Platform. The basin can be divided into six tectonic units: the Yimeng Uplift, the Jinxi Fault Belt, the Weibei Uplift, the Tianhuan Depression, the Western Thrust Belt and the Yishan Slope. The working area is located in the northwestern part of the basin, and the target layer is the tight shale-oil deposit in the Chang-7 part of the Yanchang Formation. The formation rocks consist of interbedded sandstone and shale. The diagenetic grains have good sorting and medium roundness (subangular).

Mineral components and observed correlations

Ten sandstone samples are taken from the target layer. They are processed and formed into cylinders with a diameter of 25.2 mm and a length of less than 50 mm. Then XRD and CTS tests are performed to analyze the mineralogy and pore structure. Table 1 shows the mineral composition, with samples consisting of quartz, feldspar, carbonates, clay minerals and a small amount of iron ore. The feldspars are mainly plagioclase and K-feldspar, with a higher percentage of plagioclase, and the iron ores are mainly siderite. Fig. 1 shows the thin sections of samples C and I. The pore space consists mainly of intergranular and microfractures, exhibiting poor connectivity and low permeability.

Table 1. Mineral composition.

Samples	Density (g/cm^3)	Porosity (%)	Quartz (%)	Feldspar (%)	Carbonate (%)	Clay (%)	Iron ore (%)
A	2.48	7.259	57.11	25.59	8.88	6.6	1.82
B	2.54	5.625	48.97	23.13	21.89	5.1	0.91
C	2.49	7.22	48.59	26.56	17.93	5.87	1.05
D	2.47	7.674	49.46	34.56	9.9	5.19	0.89
E	2.46	7.547	60.78	28.68	4.23	4.34	1.97
F	2.48	7.327	55.4	26.07	10.96	5.85	1.72
G	2.41	8.847	56.77	28.49	6.21	5.55	2.98
H	2.53	6.156	42.46	20.57	31.44	4.62	0.91
I	2.44	7.787	51.06	30.05	11.96	5.29	1.64
J	2.43	8.791	55.69	25.4	11.96	6.09	0.86

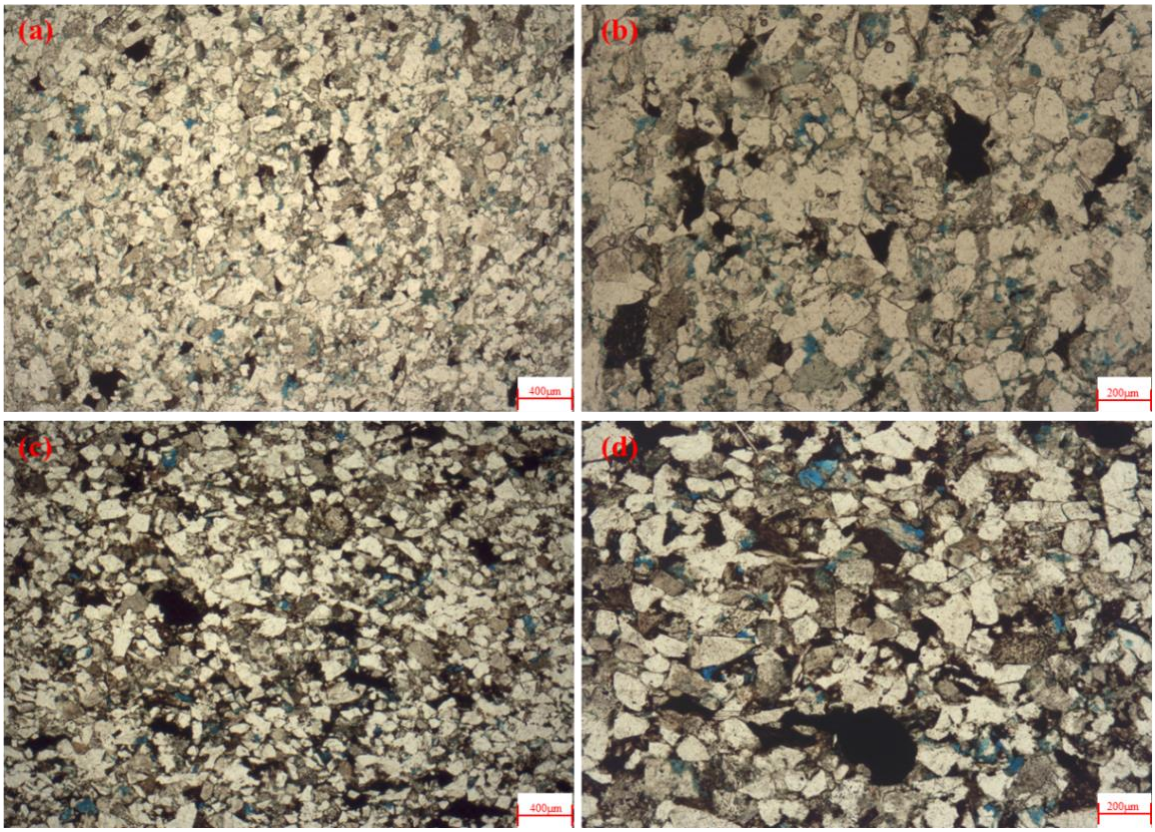

Fig. 1. Thin sections of samples C (a and b) and I (c and d) at different scales.

The minerals considered here are mainly classified into the three categories of quartz/feldspar, carbonate, and clay minerals. As are shown in Fig. 2, the samples contain high content of brittle minerals. The quartz content is 42.46%-60.78% with an average of 52.629%, feldspar 20.57%-34.56%, carbonate (calcite, dolomite) 4.23%-31.44% and clay minerals 4.34%-6.6%.

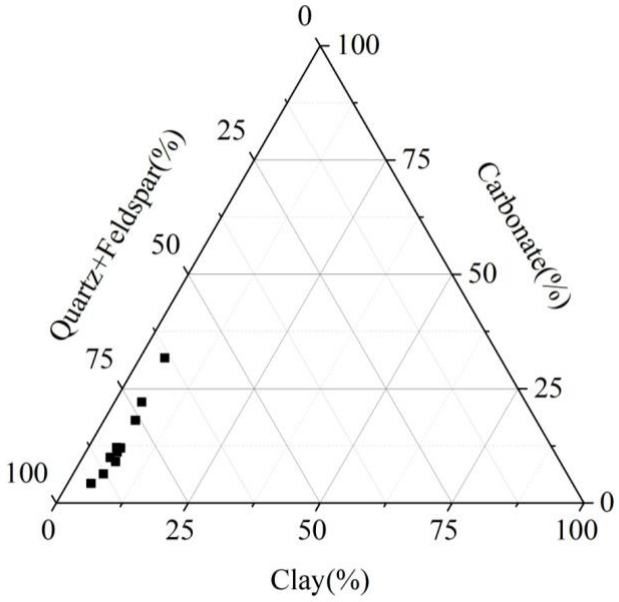

Fig. 2. Ternary plot of mineral composition of the samples of Member 7, Yanchang Formation, Ordos Basin.

Fig. 3 shows the relation between porosity and mineral content. The content of quartz+feldspar increases with porosity. There is no clear relation between clay content and porosity.

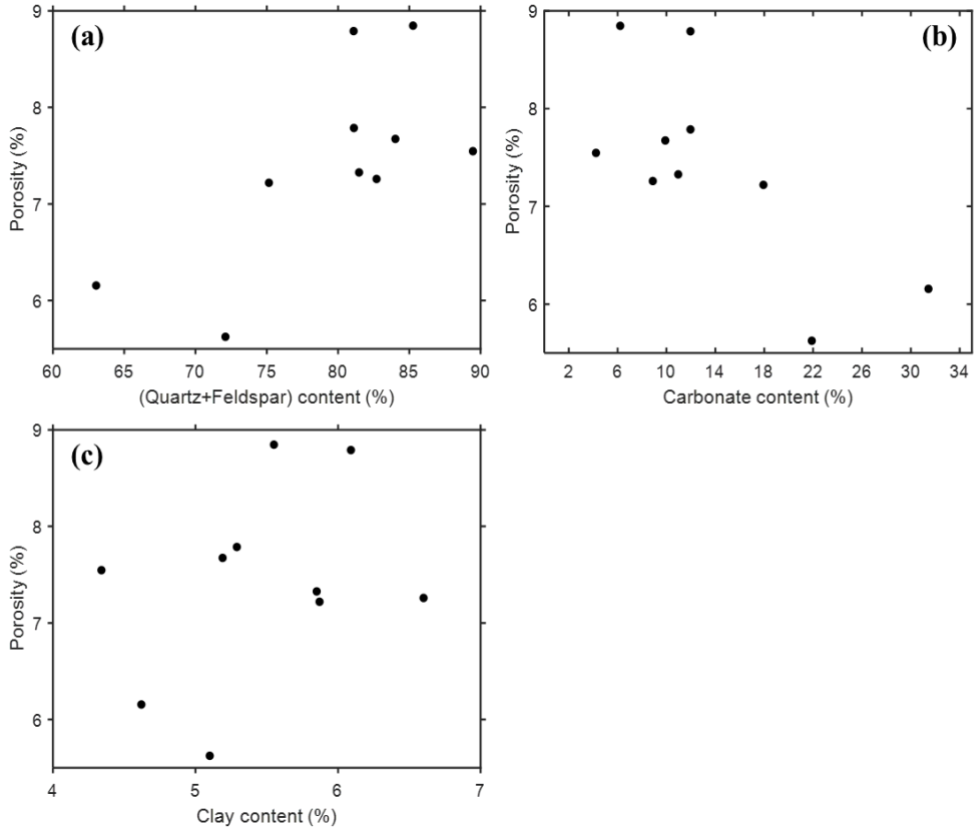

Fig. 3. Relation between porosity and mineral composition. (a) porosity/quartz+feldspar content, (b) porosity/carbonate content, (c) porosity/clay content.

Ultrasonic measurement

Ultrasonic velocities are measured by the ultrasonic pulse transmission method. The center frequency of the pulses is 0.55 MHz. The samples are dried in an oven and then saturated with oil. Then they are sealed with a rubber jacket and placed in the container. The test temperature is 20 °C and the pore pressure is 15 MPa. The P-wave quality factors of the samples are estimated by the spectral-ratio method, with a standard from an aluminum rod as a reference (Toksöz, 1979; Guo et al., 2006).

$$\ln\left[\frac{A_1(f)}{A_2(f)}\right] = -\frac{\pi x}{QV} f + \ln\left[\frac{G_1(f)}{G_2(f)}\right], \tag{1}$$

where f is frequency, $A_1(f)$ and $A_2(f)$ are the amplitude spectra of the sample and reference, respectively, Q is the quality factor, x is the wave propagation distance, V is the wave velocity, and $G_1(f)$ and $G_2(f)$ are the geometry factors of the sample and reference, respectively.

Fig. 4 shows that the measured V_P and V_S (obtained by picking the first arrivals) decrease with increasing porosity, and the P-wave attenuation (1000/Q) increases with increasing porosity.

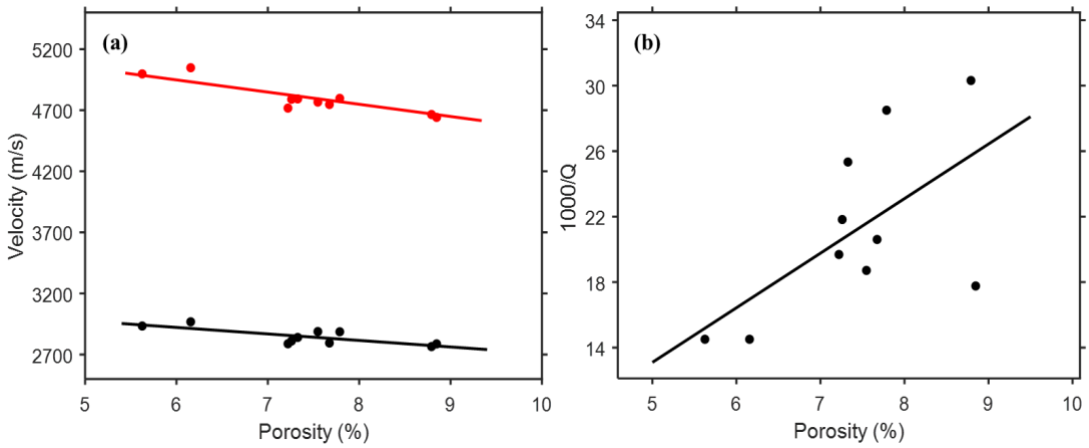

Fig. 4. (a) V_P (red) and V_S (black) as a function of porosity, measured in the ultrasonic tests. (b) 1000/Q as a function of porosity.

Well-log data

Log curves for the target layer of well B are shown in Figure 5, including porosity (ϕ), P-wave (V_P) and S-wave velocities (V_S), Poisson's ratio (υ), and natural gamma (GR), where the sandstone layer is indicated. Sonic-log attenuation is obtained with the centroid frequency-shift method of Quan and Harris (1997), by assuming that the amplitude spectrum of the wavelet is consistent with the Gaussian shape. The quality factor Q can be determined as

$$Q = \frac{\pi t \sigma_0^2}{f_{C0} - f_{C1}}, \tag{2}$$

where f_{C0} and f_{C1} are the signal centroid frequencies before and after attenuation, respectively, σ_0^2 denotes the variance of the signal before attenuation, and t is the travel time.

Apparent differences in responses are observed in the sandstone and shale sections. The range of variation in natural gamma values and P-wave attenuation (1000/Q) in the shale section is relatively large. In Fig. 6, V_P and V_S decrease with clay content. However, the brittleness index (determined according to Appendix B) and Poisson's ratio do not show a clear relationship with clay content. The target layer is divided into sandstone and shale sections, and the modeling and reservoir identification are performed according to the lithology.

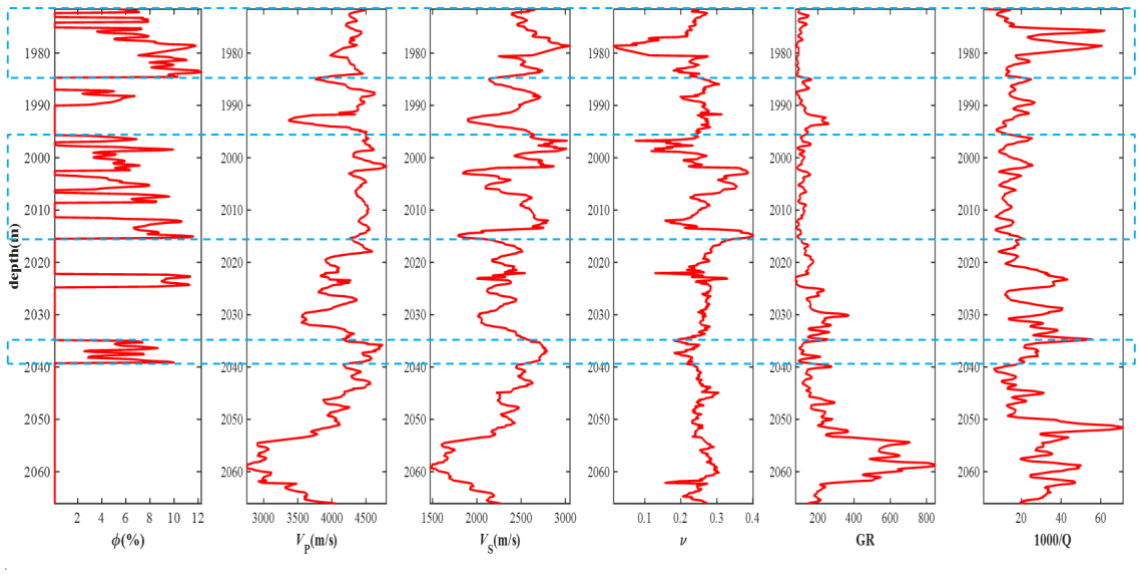

Fig. 5. Log data of the shale-oil formations corresponding to well B. The columns from left to right represent ϕ, V_P, V_S, υ, GR, and 1000/Q.

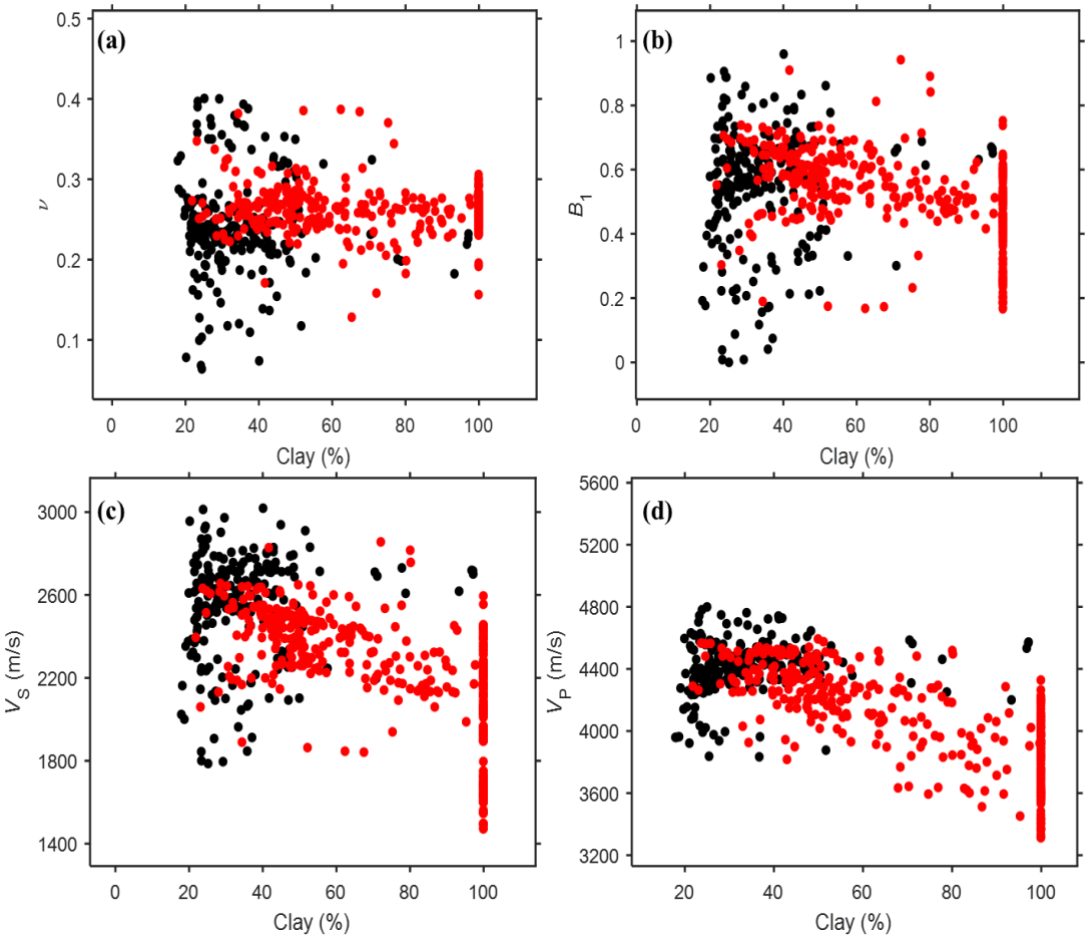

Fig. 6. Relations between clay content and Poisson's ratio (a), brittleness index B_1 (b), and P- (c) and S-wave velocities (d) for the log data. Black circles represent sandstone and red circles shale.

Seismic-attenuation estimation

Traditional methods for estimating attenuation in the frequency domain include the centroid frequency-shift method and the peak frequency-shift method. The difficulty lies in the accuracy of the estimation and the insufficient time-frequency resolution in the seismic data of tight reservoirs. An improved frequency shift method proposed by Tu et al. (2009), Hu et al. (2013), and Li et al. (2015) is used, which combines the advantages of the two methods and provides higher accuracy of Q estimation with better stability and applicability, such as

$$Q = \frac{\sqrt{\pi^5} t f_{C1} f_{C0}^2}{16(f_{C0}^2 - f_{C1}^2)}. \tag{3}$$

Fig. 7(a) shows the seismic-amplitude profile of the target formations of the survey line crossing wells A, B and C, and Fig. 7(b) shows the attenuation (1000/Q). The upper section is the sandstone section and the lower one the shale section. The results indicate that the rocks at wells A and B exhibit significant attenuation.

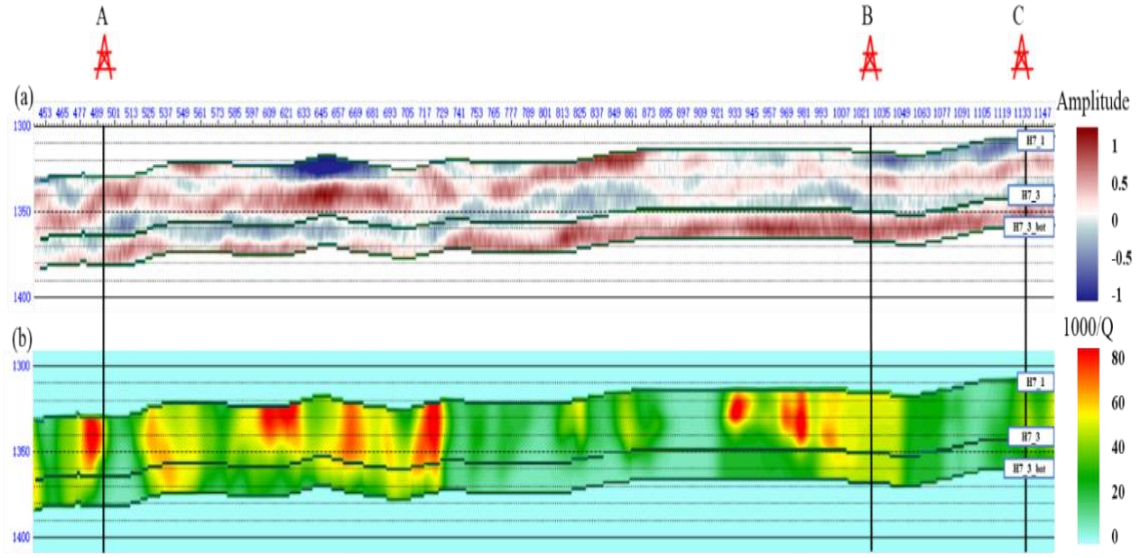

Fig. 7. 2D profiles of seismic amplitude (a) and attenuation (b).

Rock-physics model

The rocks of the sandstone section are composed of quartz, feldspar, clay, carbonate, and iron ore. The shale rocks are composed mainly of clay, quartz, feldspar, and carbonate minerals. We assume that the pores are mainly contained in the host phase of the quartz. RPMs are determined by using the Voigt-Reuss-Hill (VRH) average, the self-consistent approximation (SCA) and differential effective medium (DEM) theories, the squirt-flow model

(Gurevich et al., 2010), and the Gassmann equation (Gassmann, 1951), which are listed in Appendix A. According to the thin sections of sandstones and the analytical results, clay minerals are mainly distributed around the grains. Clay minerals in shales are the main supporting minerals that form the matrix and skeleton (Shi et al., 2021; Pang et al., 2022). Figs. 8 and 9 show the workflows. The mineral parameters are listed in Table 2.

RPM of the sandstone

Pores with a given aspect ratio are added in quartz minerals with the DEM theory to calculate the elastic moduli of the dry skeleton. The elastic moduli of the mixed feldspar, carbonate, and iron ore minerals are obtained with the VRH average. The elastic moduli of rock skeleton are determined according to SCA theory. Next, DEM is used by adding microcracks into the rock skeleton as inclusions with different aspect ratios. Then we add clay minerals with fixed aspect ratio into the skeleton with DEM. The elastic properties of the rocks are obtained by using the squirt-flow model and the Gassmann equation.

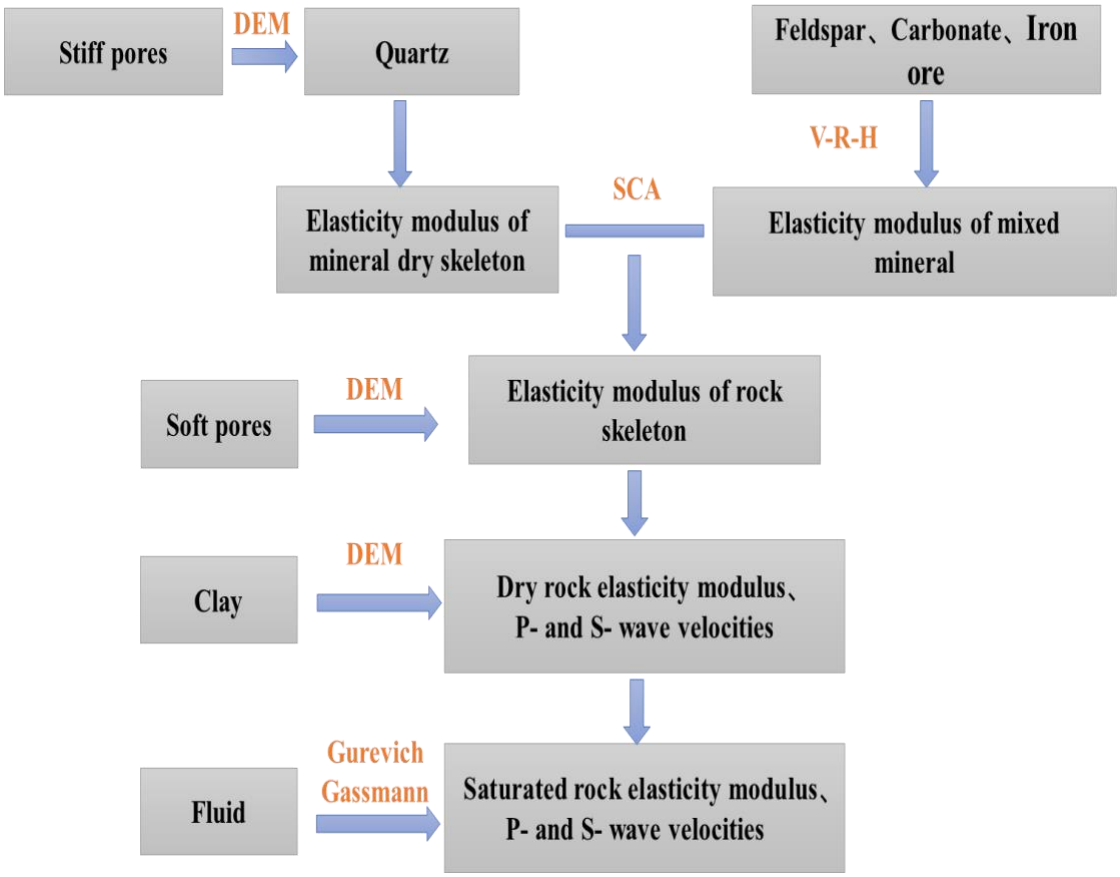

Fig. 8. Rock-physics modeling flowchart of the sandstone.

RPM of the shale

Similarly, in DEM theory, stiff pores are embedded in quartz minerals. The elastic moduli of the mixture of clay, feldspar and carbonate minerals are determined by VRH, while the elastic moduli of the rock skeleton are determined by SCA. Microcracks are added into the skeleton as inclusions with different aspect ratios, and then we obtain the elastic parameters.

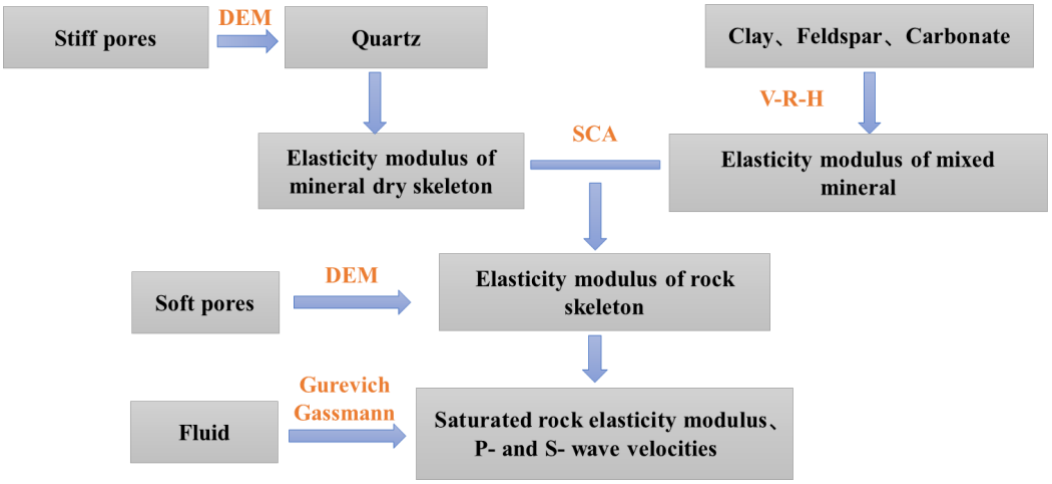

Fig. 9. Rock-physics modeling flowchart of the shale.

Table 2. Mineral properties.

Mineral	Density (g/cm^3)	Bulk modulus (Gpa)	Shear modulus (Gpa)
Quartz	2.65	37	44
Feldspar	2.62	37.5	15
Clay	2.6	21	7
Calcite	2.71	76.8	32
Dolomite	2.87	94.9	45
Siderite	3.96	123.7	51

Wave velocities and attenuation

Modeling is performed to estimate the P-wave velocity and attenuation of sandstone (Fig. 10) and shale (Fig. 11) as a function of frequency for different total/microcrack porosities and clay contents. The P-wave velocity decreases with increasing porosity, microcrack porosity and clay content. Dispersion and attenuation increase with porosity and microcrack porosity, but the effect of clay is smaller.

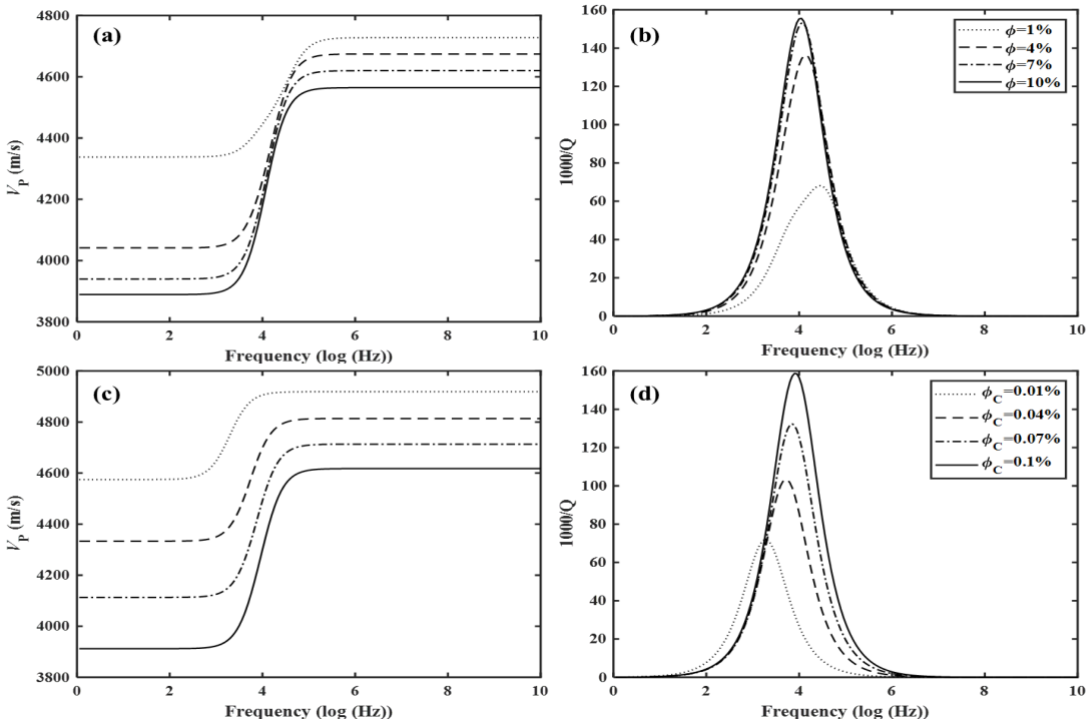

Fig. 10. P-wave velocity (a) and attenuation (b) of the sandstone layer as a function of frequency for different porosities (microcrack porosity ϕ_C = 0.1%). P-wave velocity (c) and attenuation (d) with as a function of frequency for different microcrack porosities (porosity ϕ = 10%).

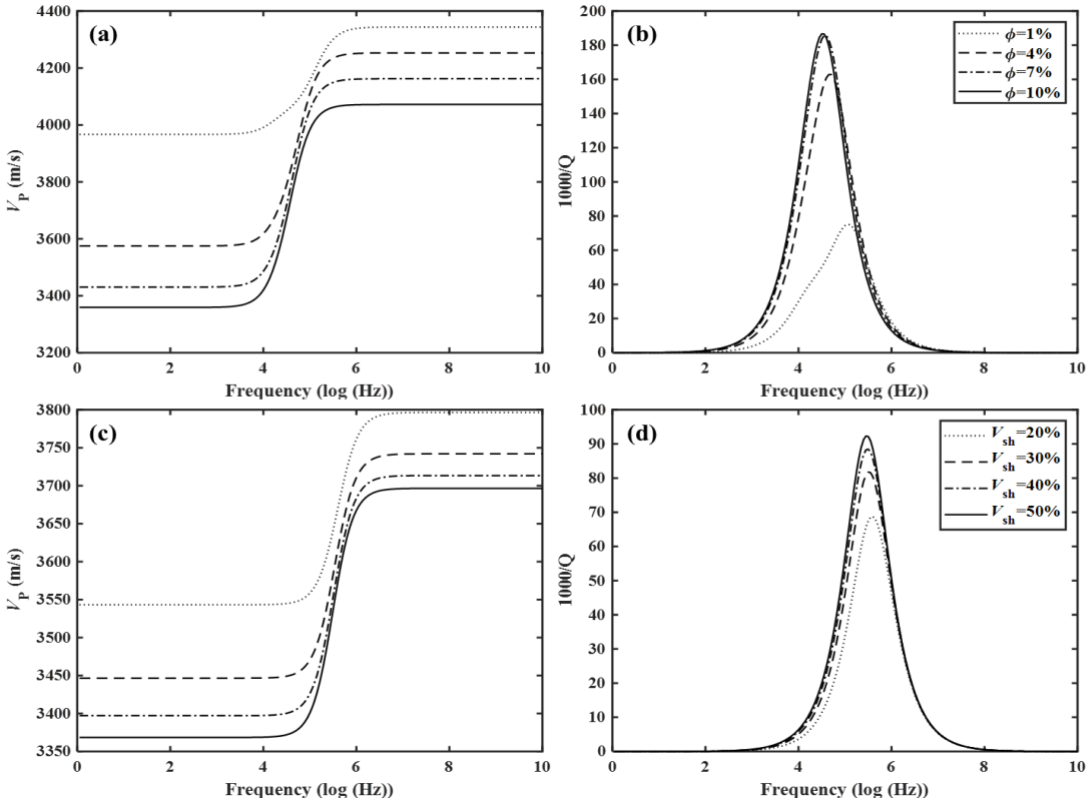

Fig. 11. P-wave velocity (a) and attenuation (b) of the shale layer as a function of frequency for different porosities (ϕ_C = 0.1%). P-wave velocity (c) and attenuation (d) as a function of frequency for different clay contents (ϕ = 10%, ϕ_C = 0.1%).

Fig. 12 shows the comparison between the P- and S-wave velocities predicted by RPM and those from ultrasonic measurements for the sandstones. The model results and measured data agree well. The discrepancies are related to the idealized and fixed geometries in the modeling, and there are different pore structures in different rocks.

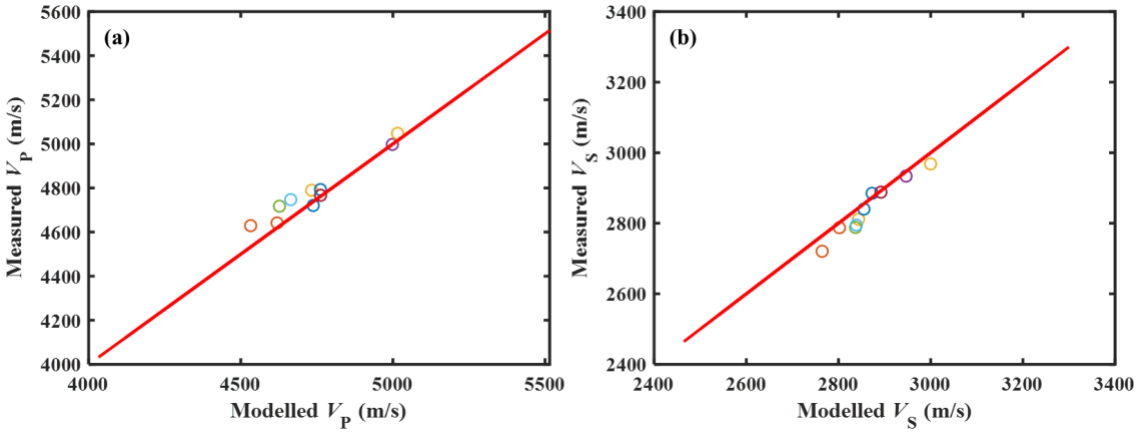

Fig. 12. Comparison between the measured V_P and the modeled V_P (a), and the same for V_S (b).

3D rock-physics template

The rock-physics template provides the relationships between mineral composition, porosity and elastic properties. 3D RPT is created based on the modeling to predict the reservoir properties by using ultrasonic, log and seismic data. In the sandstone section, the template is given when the quartz content increases from 20% to 60% and the feldspar content decreases from 60% to 20%. The clay content and carbonate minerals at 10%. In the shale section, the template is given when the quartz content increases from 10% to 50% and the clay content decreases from 70% to 30%, The feldspar content and carbonate minerals are set to 10%. The 3D RPTs of sandstone and shale at different frequencies are plotted in terms of attenuation, P-wave impedance (I_P) and V_P/V_S.

3D RPTs at the ultrasonic frequency band

As is shown in Figs. 13 and 14, porosity is 1%-10% and microcrack aspect ratio 10^{-3}-10^{-2}. At constant quartz content and microcrack aspect ratio, attenuation increases with increasing porosity, while I_P and V_P /V_S decrease with porosity. For the constant quartz content and porosity, attenuation, I_P and V_P /V_S increase with increasing microcrack aspect ratio. At constant porosity and microcrack aspect ratio, attenuation and V_P /V_S decrease with increasing of quartz content, while I_P increases with quartz content. The ultrasonic template is calibrated based on the measurements of the ten sandstone samples. The porosity and quartz content of the samples agree well with the template.

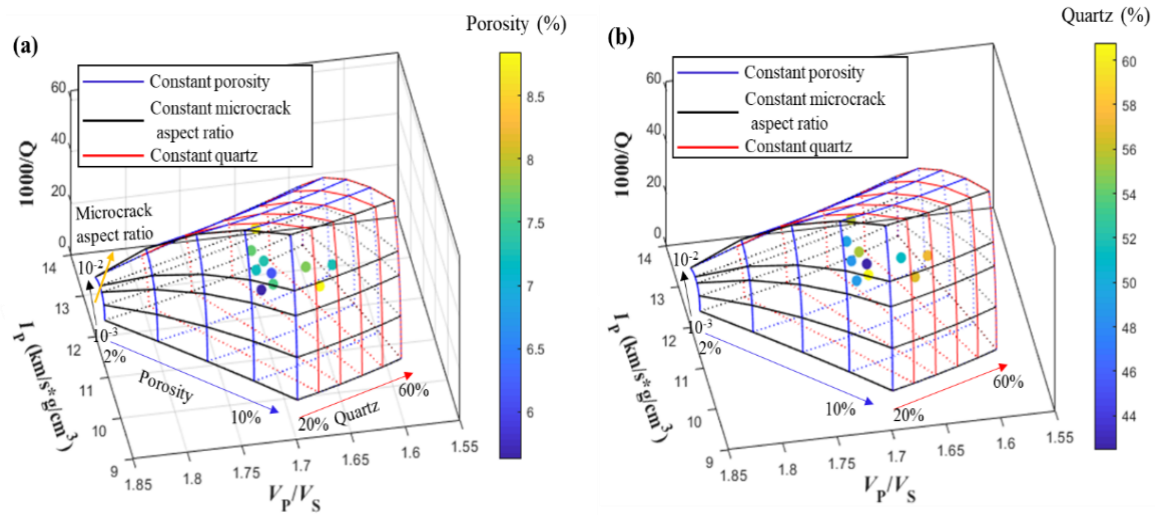

Fig. 13. 3D RPTs at 0.55 MHz of the sandstone showing the effects of quartz content, porosity and aspect ratio on I_P, V_P /V_S and 1000/Q. The colorbar indicates porosity (a) and quartz content (b).

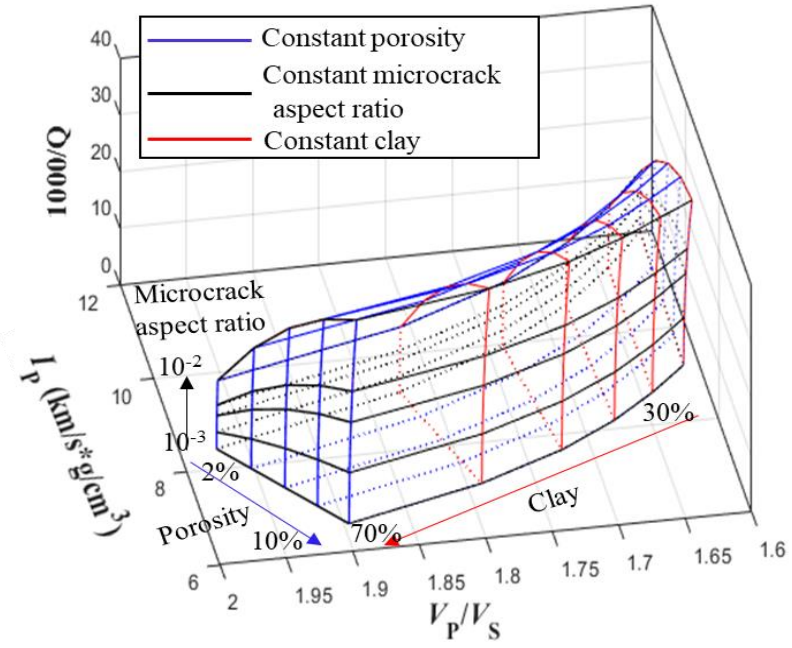

Fig. 14. 3D RPT at 0.55 MHz of the shale showing the effects of quartz content, porosity and aspect ratio on I_P, V_P /V_S and 1000/Q.

3D RPTs with well-log data

With a porosity of 1%-10% and a microcrack aspect ratio of 10^{-4}-10^{-3}, Figs. 15 and 16 show the application of RPTs based on log data. The brittleness index B_1 is estimated according to Appendix B. The trend is generally consistent with that in the ultrasonic frequency range. Most data are distributed within the templates. As the quartz content increases, the brittleness index B_1 increases, indicating higher brittleness.

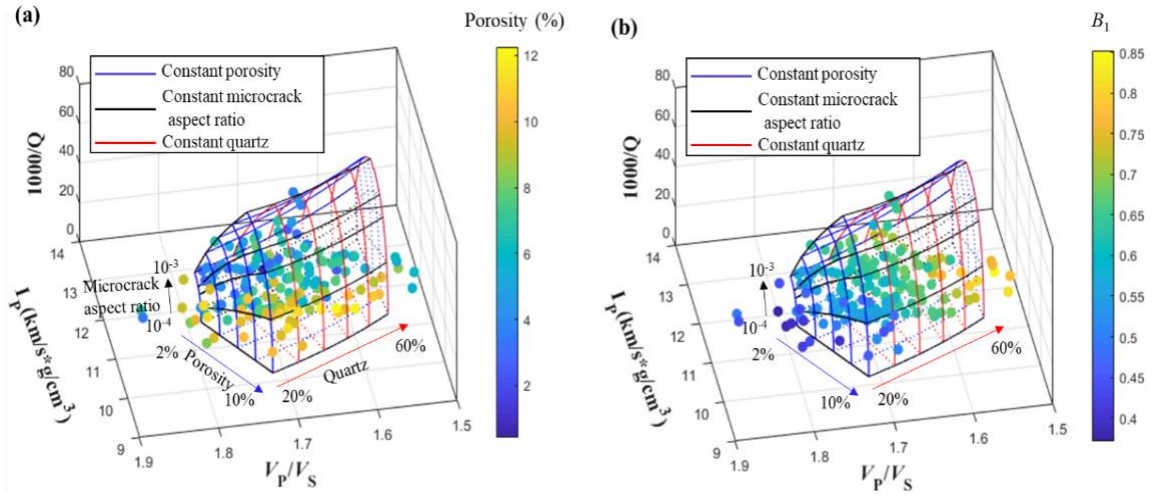

Fig. 15. 3D RPTs of the sandstone based on well-log data. The colorbar indicates porosity (a) and B_1 (b).

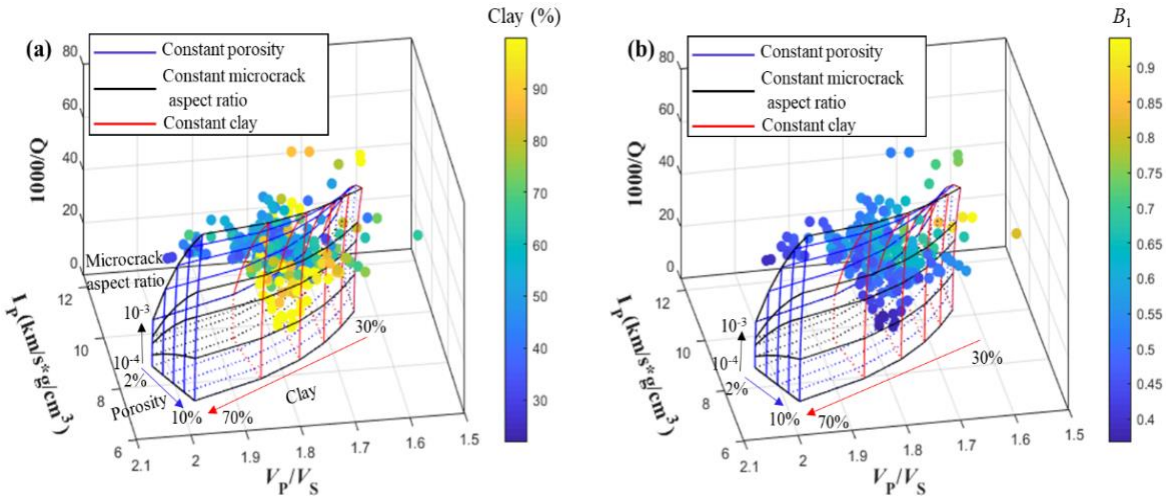

Fig. 16. 3D RPTs of shale based on well-log data. The colorbar indicates clay content (a) and B_1 (b).

3D RPTs at the seismic frequency range

Figs. 17 and 18 show the RPTs of the seismic frequency band, with porosity of 1%-10% and microcrack aspect ratio of 10^{-5}-10^{-4}. The seismic data are used to estimate attenuation with eq. (3), and I_P and V_P /V_S are obtained from pre-stack inversion. The attenuation, I_P and V_P /V_S of the seismic traces around the well, and the porosity of the log data (resampled according to the seismic data) are considered. It is shown that the data sets are essentially consistent with the template, and the attenuation gradually increases with porosity.

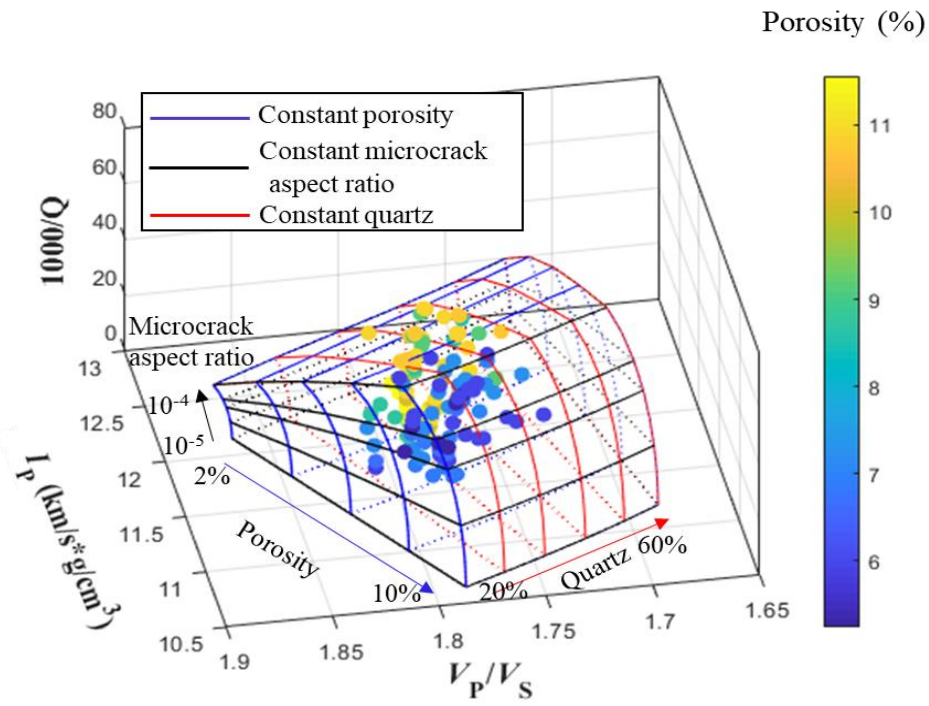

Fig. 17. 3D RPT at 35 Hz of the sandstone and seismic data (scatters). The colorbar indicates the porosity.

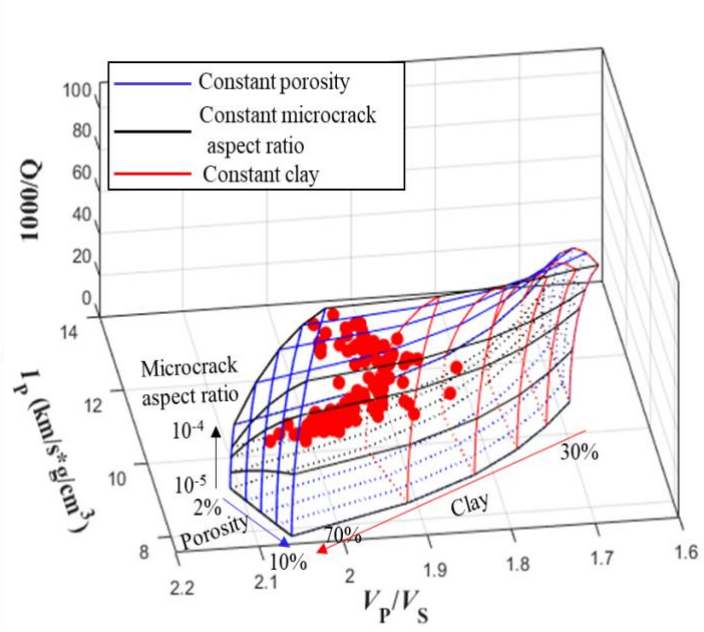

Fig. 18. 3D RPT at 35 Hz of the shale and seismic data (scatters).

Reservoir property prediction with seismic data

Based on the seismic-scale RPT, the sandstone section has relatively high P-wave impedances and low V_P /V_S ratios, compared to the shale section. The seismic inversion data are compared with the 2D RPT of I_P and V_P /V_S for sandstone and shale sections, as are shown in Fig. 19. The seismic data for the two lithologies can be well distinguished with a fitting line,

combined with the templates. Then, the seismic inversion data and reservoir parameters for the two lithologies are obtained, with the upper section corresponding to the sandstone section of Chang 7-1 and Chang 7-2 layers, and the lower section corresponding to Chang 7-3 shale.

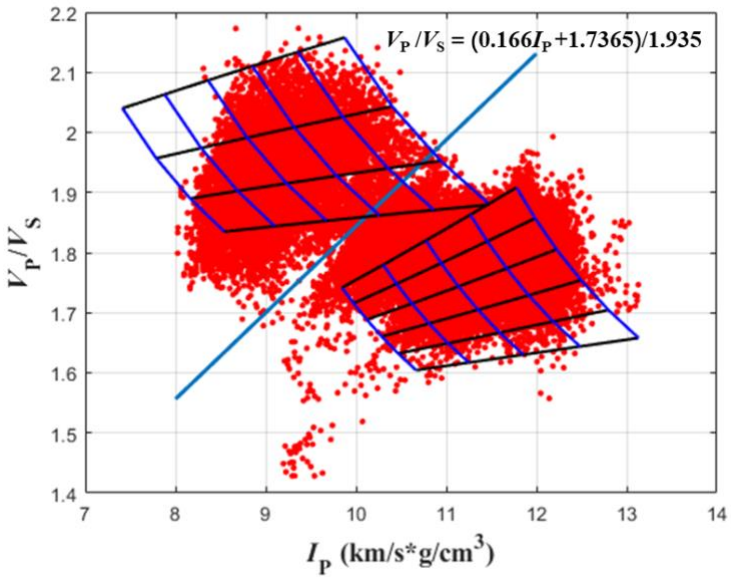

Fig. 19. Seismic data for the sandstone and shale layers (scatters).

Fig. 20 shows the 2D seismic inversion of P-wave impedance and V_P/V_S crossing wells A, B, and C. The upper layer of Chang 7-1 and Chang 7-2 is mainly sandstone, while the lower layer contains shale. First, the data are divided into sandstone and shale sections. Then, within the area of each template, the grid points on the 3D template closest to the data scatters (I_P, V_P/V_S ratio and attenuation) are considered, and the quartz content, porosity and microcrack aspect ratio are determined. Quantitative prediction of these survey line parameters can be helpful in reservoir interpretation. The predictions are shown in Fig. 21.

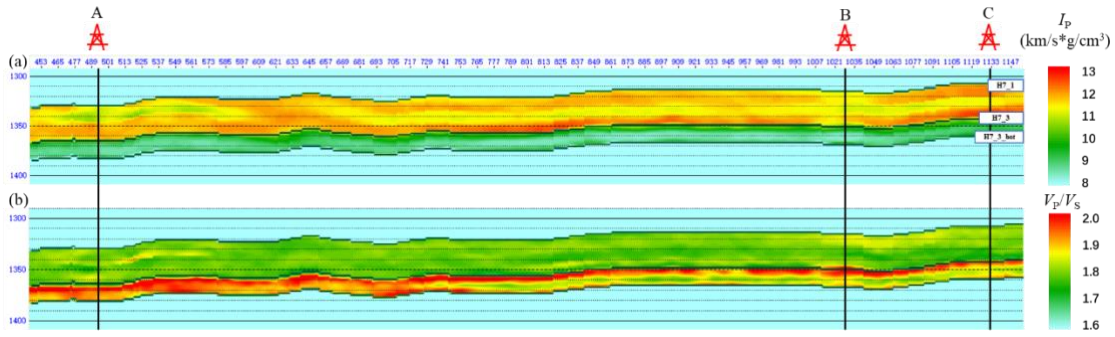

Fig. 20. Inversion of a 2D seismic line crossing wells A, B and C. (a) P-wave impedance. (b) V_P/V_S.

Fig. 21 shows the 2D profiles of quartz content, porosity, and microcrack aspect ratio. The target formation is quite tight, which is consistent with the regional geological studies. The results show that the

upper layer (mainly tight sandstone) has higher porosity and quartz content, while the lower layer (shale) has lower quartz content and higher clay content. Fig. 21 (d) shows the spatial distribution of the brittleness index for boreholes A, B, and C obtained with using Appendix B. It can be observed that the quartz content and porosity predictions are related to the brittleness index. However, there is no clear correlation between the predicted microcrack aspect ratio and the brittleness index. Well B is located in the high porosity and high quartz zone. From the oil production report of well B, the cumulative production was 528.7 tons, while wells A and C showed low production. The prediction results are consistent with actual production conditions.

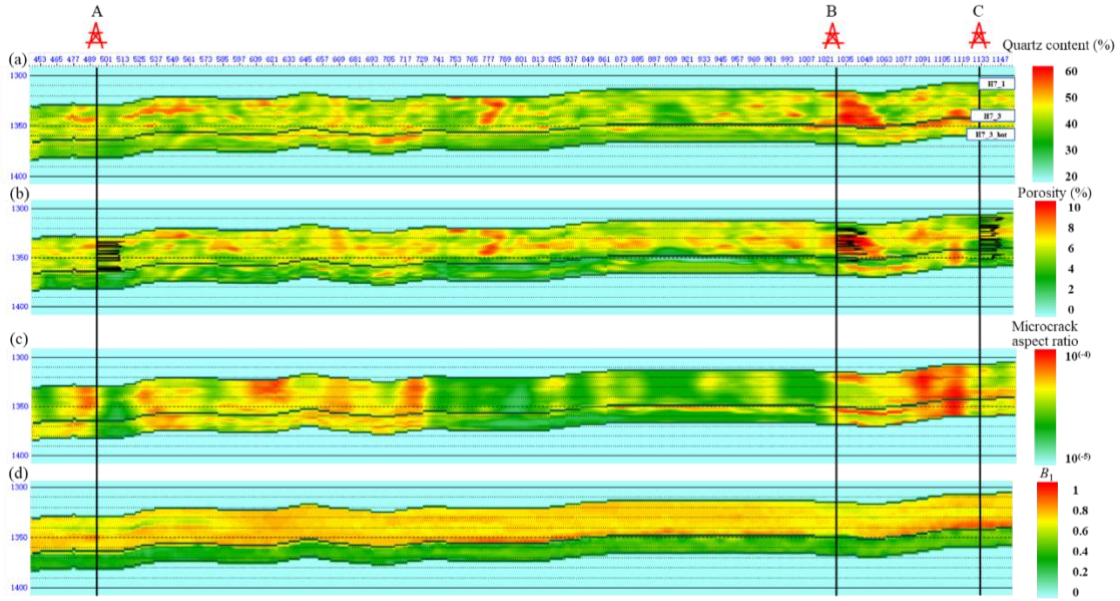

Fig. 21. The predictions of wells A, B and C. (a) quartz content from the RPM; (b) porosity from the RPM (the log curves give porosities); (c) microcrack aspect ratio from the RPM; (d) brittleness index.

CONCLUSIONS

The rock-physics properties and pore structures for the shale-oil formations of the Chang-7 member of the Ordos Basin are analyzed based on XRD, CTS and ultrasonic investigations. By using the VRH, SCA, and DEM equations, squirt-flow model and Gassmann equation, the RPMs of the target sandstone and shale sections are built. We consider quartz as the host phase. Based on the modeling, the effects of porosity, mineral composition, and microcrack aspect ratio on the wave responses and attenuation are analyzed. The 3D RPTs of the two lithologies are built to estimate the reservoir properties and interpret ultrasonic, log and seismic data. The study shows that the shale layer has lower quartz content and porosity, which is consistent with the actual geological properties. Brittleness is related to mineral composition and porosity. Higher brittleness is associated with higher quartz content. V_P/V_S ratio, P-wave impedance and attenuation are the indicators of porosity, quartz content and microcrack aspect ratio in the target formations.

With using the RPTs, the seismic data for the sandstone and shale sections of the Chang 7 deposits are differentiated and the estimation of the properties for the two lithologies are presented. The results show that these estimated attributes are consistent with the actual oil production reports. The proposed RPMs can provide technical support for shale attribute estimation and guidance for further reservoir engineering applications.

ACKNOWLEDGEMENTS

This work is supported by the National Natural Science Foundation of China (41974123 and 41704109), and the Jiangsu Province Science Fund for Distinguished Young Scholars (BK20200021).

Appendix A: Theoretical models

We use the Voigt-Reuss-Hill average, the self-consistent approximation (SCA), the differential effective medium (DEM), the squirt flow model (Gurevich et al., 2010) and the model of Gassmann (1951) to build the rock-physics models.

Voigt-Reuss-Hill average

The Voigt (1928) bound is sometimes referred to as the average value for equal strains because it gives the ratio between the average stress and the average strain when the components are assumed to have equal strains. The Reuss bound (1929) is called the average value for equal stresses because it gives the ratio between average stress and average strain when the components are assumed to have equal stresses. Hill (1952) suggested taking the average of the results of the two models:

$$M_V = \sum_{i=1}^{N} f_i M_i , \tag{A-1}$$

$$\frac{1}{M_R} = \sum_{i=1}^{N} \frac{f_i}{M_i} , \tag{A-2}$$

$$M_{VRH} = \frac{M_V + M_R}{2} , \tag{A-3}$$

where M_V, M_R and M_{VRH} are Voigt, Reuss and Voigt-Reuss Hill averages, respectively, with i indicating mineral phase, f_i volume fraction and M_i the corresponding elastic modulus of the N phases.

Self-consistent model

Based on the elastic wave scattering theory, Berryman (1980, 1992 and 1998) proposed a general form of the self-consistent approximation for n-phase mixtures,

$$\sum \chi_i (K_i - K^*_{SC}) P^{*i} = 0 , \tag{A-4}$$

$$\sum \chi_i(\mu_i - \mu^*_{SC})Q^{*i} = 0, \tag{A-5}$$

where i indicates the mineral phase or pore space with a corresponding volume fraction χ_i, bulk modulus K_i and shear modulus μ_i. The factors P^{*i} and Q^{*i} describe the geometrical shape of an inclusion corresponding to phase i.

Differential effective medium

The differential effective medium (DEM) theory was established for biphasic mixtures by gradually adding inclusions into solid mineral phases (Norris et al.,1985; Zimmerman. 1991). The coupled differential equations for the effective bulk and shear moduli (Berryman, 1992) are

$$(1-y)\frac{\mathrm{d}}{\mathrm{d}y}[K^*(y)] = (K_2 - K^*)P^{(*2)}(y), \tag{A-6}$$

$$(1-y)\frac{\mathrm{d}}{\mathrm{d}y}[\mu^*(y)] = (\mu_2 - \mu^*)Q^{(*2)}(y), \tag{A-7}$$

with $K^*(0) = K_1$ and $\mu^*(0) = \mu_1$, where K_1 and μ_1 are the bulk and shear moduli of the initial host phase material (phase 1), respectively, K_2 and μ_2 are the bulk and shear moduli of the gradually added inclusions (phase 2), respectively, and y represents the content of phase 2.

Squirt-flow model

Gurevich et al. (2010) proposed a squirt-flow model that describes the squirt-flow effects, where compliant (soft) pores connected to stiff pores act as fluid channels. The dry-rock bulk and shear moduli (K_{bf} and μ_{bf}) including squirt flow effects, are calculated as

$$\frac{1}{K_{bf}} = \frac{1}{K_h} + \left(\frac{1}{\frac{1}{K_{dry}} - \frac{1}{K_h}} + \frac{3\omega i\eta}{8\phi_C\alpha_C} \right)^{-1}, \tag{A-8}$$

$$\frac{1}{\mu_{bf}} = \frac{1}{\mu_{dry}} - \frac{4}{15}\left(\frac{1}{K_{dry}} - \frac{1}{K_{bf}} \right), \tag{A-9}$$

where η is the fluid viscosity, ω is the angular frequency, and α_C is the microcrack aspect ratio. Moreover, K_h is the bulk modulus of the frame containing only stiff pores, and K_{dry} and μ_{dry} represent the bulk and shear moduli obtained with the DEM equations, respectively.

Gassmann equation

Gassmann (1951) established an equation defining the relationship between the stiffnesses of the different components of a porous medium at the low frequency limit. This relation is

$$\frac{K_{sat}}{K-K_{sat}}=\frac{K_{dry}}{K-K_{dry}}+\frac{K_{fl}}{(K-K_{fl})\phi}, \tag{A-10}$$

$$\mu_{sat}=\mu_{dry}, \tag{A-11}$$

where K_{sat} and K_{dry} are the wet-rock and dry-rock bulk moduli, respectively, K and K_{fl} are the bulk moduli of the mineral mixture and pore fluid, respectively, μ_{sat} and μ_{dry} are the wet-rock and dry-rock shear moduli, respectively, and ϕ is the porosity.

Wave velocities and quality factors of the saturated rock

$$V_{\mathrm{S}}=\sqrt{\frac{\mu_{bf}}{\rho_{sat}}}, \tag{A12}$$

$$V_{\mathrm{P}}=\sqrt{\left(\frac{4}{3}V_{\mathrm{S}}^{2}+\frac{K_{sat}}{\rho_{sat}}\right)}, \tag{A13}$$

$$Q=\frac{\mathrm{Re}\left(K_{sat}+4\mu_{bf}/3\right)}{\mathrm{Im}\left(K_{sat}+4\mu_{bf}/3\right)}, \tag{A14}$$

where ρ_{sat} is density of saturated rock.

Appendix B: Brittleness index

Rickman (2008) considered that high brittleness corresponds to high Young modulus and low Poisson ratio. The brittleness index B_1 is

$$B_1=\frac{E_{BI}+\upsilon_{BI}}{2}, \tag{B-1}$$

$$\upsilon_{BI}=\frac{\upsilon-\upsilon_{\max}}{\upsilon_{\min}-\upsilon_{\max}}, \tag{B-2}$$

$$E_{BI}=\frac{E-E_{\min}}{E_{\max}-E_{\min}}, \tag{B-3}$$

where E is Young's modulus, υ is Poisson's ratio, $E_{\max}$ ($\upsilon_{\max}$) and $E_{\min}$ ($\upsilon_{\min}$) are the maximum and minimum values, respectively, and E_{BI} and υ_{BI} are the corresponding normalized quantities.

REFERENCES

Ba, J., Hu, P., Tan, W., Müller T.M. and Fu, L., 2021. Brittle mineral prediction based on rock physics modeling for tight oil reservoir rocks. J. Geophys. Engineer., 18: 970-983.

Ba, J., Xu, W., Fu, L., Carcione, J.M. and Zhang, L, 2017. Rock anelasticity due to patchy-saturation and fabric heterogeneity: A double-double porosity model of wave propagation. J. Geophys. Res., Solid Earth, 122: 1949-1976.

Ba, J., Cao, H., Carcione, J.M., Tang, G., Yan, X., Sun, W. and Nie, J., 2013a. Multiscale rock-physics templates for gas detection in carbonate reservoirs. J. Appl. Geophys., 93: 77-82.

Ba, J., Yan, X., Chen, Z., Xu, G., Bian, C., Cao, H., Yao, F. and Sun, W., 2013b. Rock physics model and gas saturation inversion for heterogeneous gas reservoirs. Chin. J. Geophys. (in Chinese), 56: 1696-1706.

Berryman, J.G., 1980. Long wavelength propagation in composite elastic media II. Ellipsoidal inclusions. J. Acoust. Soc. Am., 68: 1820-1831.

Berryman, J.G.. 1992. Single-scattering approximations for coefficients in Biot's equations of poroelasticity. J. Acoust. Soc. Am., 91: 551-571.

Berryman, J.G., 1998. Long-wavelength propagation in composite elastic media I. Spherical inclusions. J. Acoust. Soc. Am.: 68, 1809-1819.

Carcione, J.M. and Avseth, P., 2015. Rock-physics templates for clay-rich source rocks. Geophysics, 80 (5), D481-D500.

Carcione, J.M., Helle, H.B. and Pham, N.H., 2003. White's model for wave propagation in partially saturated rocks. Comparison with poroelastic numerical experiments. Geophysics, 68: 1389-1398.

Chapman, S., Tisato, N., Quintal, B. and Holliger, K., 2016. Seismic attenuation in partially saturated Berea sandstone submitted to a range of confining pressures. J. Geophys. Res., Solid Earth: 121: 1664-1676.

Chen, J., Zhang, G., Chen, H. and Yin, X.Y., 2014. The construction of shale rock physics effective model and prediction of rock brittleness. Expanded Abstr., 84th Ann. Internat. SEG Mtg.,, Denver: 2861-2865.

Cilli, P. and Chapman, M., 2021. Linking elastic and electrical properties of rocks using cross-property DEM. Geophys. J. Internat., 225: 1812-1823.

Dasgupta, R. and Clark, R.A., 1998. Estimation of Q from surface seismic reflection data. Geophysics, 63: 2120-2128.

Deng, J., Wang, H., Zhou, H., Liu, Z., Song, L. and Wang, X., 2015. Microtexture, seismic rock physical properties and modeling of Longmaxi Formation shale. Chin. J. Geophys. – Chin. Ed., 58: 2123-2136.

Dutilleul, J., Bourlange, S., Géraud, Y. and Stemmelen, D., 2020. Porosity, pore structure, and fluid distribution in the sediments entering the northern Hikurangi margin, New Zealand. J. Geophys. Res., Solid Earth, 125(11).

Dvorkin, J. and Mavko, G., 2006. Modeling attenuation in reservoir and nonreservoir rock, The Leading Edge, 25: 194-197.

Fan, J.F., Shi, J., Wan, X., Xie, Q. and Wang, C., 2022. Classification evaluation method for Chang 7 oil group of Yanchang formation in Ordos Basin. J. Petrol. Explor. and Product. Technol., 12: 825-834.

Feng, S., Niu, X., Liu, F. and Yang, X., 2013. Characteristics of Chang7 tight oil reservoir space in Ordos basin and its significance. J Centr. South Univ., 44: 4574-4580.

Gassmann, F., 1951. Elasticity of porous media: Vierteljahrsschrder Naturforschenden Gesselschaft, 96: 1-23.

Guo, M. and Fu, L., 2006. Stress associated coda attenuation from ultrasonic waveform measurements. Geophys. Res. Lett., 34: L09307.

Guo, Z., Li, X., Liu, C., Feng, X. and Shen, Y., 2013. A shale rock physics model for analysis of brittleness index, mineralogy and porosity in the Barnett Shale. J. Geophys. Engineer., 10, 025006.

Gupta, S.D., Chatterjee, R. and Farooqui, M.Y., 2012. Rock physics template (RPT) analysis of well logs and seismic data for lithology and fluid classification in Cambay Basin. Internat. J. Earth Sci., 101: 1407-1426.

Gurevich, B., Makarynska, D., de Paula, O.B. and Pervukhina, M., 2010. A simple model for squirt-flow dispersion and attenuation in fluid-saturated granular rocks. Geophysics, 75(6), N109-N120.

Hill, R., 1952. The Elastic Behaviour of a Crystalline Aggregate. Proc. Phys. Soc.. 65: 349-354.

Hu, C., Tu, N. and Lu, W., 2013. Seismic attenuation estimation using an improved frequency-shift method. IEEE Geosci. Remote Sens. Lett., 10: 1026-1030.

Li, F., Zhou, H., Jiang, N., Bi, J. and Marfurt, K., 2015. Q estimation from reflection seismic data for hydrocarbon detection using a modified frequency shift method. J. Geophys. Engineer., 12: 577-586.

Li, H., Zhang, J., Cai, S. and Pan, H., 2019. 3D rock physics template for reservoir with complex pore structure. Chin. J. Geophys. (in Chinese), 62: 2711–2723.

Liang, X., Guan, Z., Niu, X., Guan, P., Dan, W., Feng, S. and Zhou, S., 2020. Reservoir characteristics of shale oil in Chang 7 Member of Yanchang Formation，Ordos Basin. Nat. Gas Geosci., 31: 1489-1500.

Luo. C., Ba, J. and Guo, J., 2023.Seismic petrophysical inversion with statistical double-porosity Biot-Rayleigh m odel. Geophysics, 88(3): M157-M171.

Ma, R. and Ba, J., 2020. Coda and intrinsic attenuations from ultrasonic measurements in tight siltstones. J. Geophys. Res., 125(4).

Norris, A.N., Sheng, P. and Callegari, A.J., 1985. Effective-medium theories for two-phase dielectric media. J. Appl. Phys., 57: 1990-1996.

Odegaard, E. and Avseth, P.A., 2004. Well log and seismic data analysis using rock physics templates: First Break, 22: 37- 43.

Pang, M., Ba, J., Carcione, J. M., Picotti, S., Zhou, J., Jiang, R., 2019. Estimation of porosity and fluid saturation in carbonates from rock-physics templates based on seismic Q. Geophysics, 84 (6): M25-M36.

Pang, M., Ba, J., Wu, C., Carcione, J. M., Müller, T. M., 2022. A study on acoustic-electrical properties and rock physics models for shale-oil formations: Prediction of reservoir properties of interbedded sandstone and shale layers. Applied Geophysics.

Pang, M., Ba, J., Fu, L., Carcione, J. M., Markus U., Zhang, L., 2020. Estimation of microfracture porosity in deep carbonate reservoirs based on 3D rock-physics templates. Interpretation, 8(4): SP43-SP52.

Pang, X., Jia, C., and Wang, W., 2015. Petroleum geology features and research developments of hydrocarbon accumulation in deep petroliferous basins. Pet. Sci. 12, 1-53.

Picotti, S., Carcione, J. M. and Ba, J., 2018. Rock-physics templates for seismic Q. Geophysics, 84(1), MR13-MR23.

Quan, Y. L., and Harris, J. M., 1997. Seismic attenuation tomography using the frequency shift method. Geophysics, 62(3): 895-905.

Reuss, A., 1929. Calculation of the flow limits of mixed crystals on the basis of the plasticity of monocrystals. Zeitschrift für Angewandte Mathematik, 9, 49-58.

Rickman, R., Mullen M. J., Petre J. E., Grieser W. V. and Kundert D., 2008. A practical use of shale petrophysics for stimulation design optimization: All shale plays are not clones of the Barnett shale, SPE Annual Technical Conference and Exhibition, Society of Petroleum Engineers, Denver, Colorado, USA, 21-24.

Sayers, C. M., 2005. Seismic anisotropy of shales. Geophysical Prospecting, 53:667-676.

Shi, J., Zou, Y., Cai, Y., et al., 2021. Organic matter enrichment of the Chang 7 member in the Ordos Basin: Insights from chemometrics and element geochemistry: Marine and Petroleum Geology, 135(3-4), 105404.

Spencer, J.M., and Shine, J., 2016. Seismic wave attenuation and modulus dispersion in sandstone. Geophysics, 81(3): D211-D231.

Sun, H., Duan, L., Liu, L., Fan, W., Fan, D., Yao, J., Zhang, L., Yang, Y., and Zhao, J., 2019. The influence of micro-fractures on the flow in tight oil reservoirs based on pore-network models: Energies, 12(21), 4104.

Tan, W., Ba, J., Müller, T. M., Fang, G., and Zhao, H., 2020. Rock physics model of tight oil siltstone for seismic prediction of brittleness. Geophys. Prosp.. 68:1554-1574.

Tan, W., Ba, J., Guo, M., Li, H., Zhang, L., Yu, T.and Chen, H., 2018. Brittleness characteristics of tight oil siltstones. Appl. Geophys., 15:175-187.
Toksöz, M.N., Johnston, D.H. and Timur, A., 1979. Attenuation of seismic waves in dry and saturated rocks: I. Laboratory measurements. Geophysics, 44: 681-690.
Tu, N. and Lu, W., 2009. An improved peak-frequency-shift method for Q estimation. Beijing International Geophysical Conference and Exposition.
Vernik, L., Nur, A., 1992. Ultrasonic velocity and anisotropy of hydrocarbon source rocks. Geophysics, 57(5): 727-735.
Voigt, W., 1928. Lehrbuch der Kristallphysik, p. 739.
White, J.E., 1975. Computed seismic speeds and attenuation in rocks with partial gas saturation. Geophysics, 40(2): 224-232.
Winkler, K.W., 1985. Dispersion analysis of velocity and attenuation in Berea sandstone. Journal of Geophysical Research, 90(B8): 6793-6800.
Yang, Z., He, T. and Zou, C., 2017. Shales in the Qiongzhusi and Wufeng-Longmaxi formations: a rock-physics model and analysis of the effective pore aspect ratio. Appl. Geophys., 14: 325-336.
Zhang, C.J. and Ulrych, T.J., 2002. Estimation of quality factors from CMP records. Geophysics, 67: 1542-1547.
Zhang, L., Ba, J. and Carcione, J.M., 2021. Wave propagation in infinituple-porosity media. J. Geophys. Res., Solid Earth: 126(4).
Zimmerman, R.W., 1991. Compressibility of sandstones. Developments Petroleum Science 29, 173.